Effects of acrylonitrile content and hydrogenation on fatigue behaviour of HNBR

Kubat Narynbek Ulu, Bertrand Huneau, Erwan Verron, Anne-Sophie Béranger, Patrick Heuillet

Effects of acrylonitrile content and hydrogenation on fatigue behavior of HNBR

K. Narynbek Ulu[a, 1], B. Huneau[a], E. Verron[a], A.S. Béranger[b], P. Heuillet[b]
[a]Ecole Centrale de Nantes, 1 rue de la Noë, 44321 Nantes, France
[b]LRCCP, 60 rue Auber, 94408 Vitry-sur-Seine, France

Abstract

The influence of acrylonitrile (ACN) content and hydrogenation on the fatigue properties of HNBR is investigated. HNBR blends consists of different quantities of acrylonitrile (24, 36, and 44 wt.-%) and percent hydrogenation (91, 96, and 99%), and a composite of two blends of HNBR with 24 and 44 wt.-% ACN for an average of 36 wt.-%. A comprehensive experimental campaign is carried out with fatigue life and crack propagation testing at 120 °C. Afterwards, fatigue damage is analyzed thanks to both optical and scanning electron microscopy. The results of the three experimental approaches demonstrate that HNBR with median ACN content (36 wt.-%) and median hydrogenation (96%) has the best fatigue resistance. In general, the fatigue resistance decreases in the following order: for ACN - 36 to 44 to 24 wt.-%, and for hydrogenation - 96 to 99 to 91%. The composite blend also has lower fatigue resistance than a regular HNBR blend.

Keywords: fatigue crack growth rates, fatigue damage, fatigue life, hyperelastic materials, stress control, tensile strength.

[1] Corresponding Author: kubat.narynbek-ulu@ec-nantes.fr, 1 rue de la Noe, 44321 Nantes, France Cedex

Nomenclature

c	=	crack length
dc/dN	=	fatigue crack growth rate
DIC	=	Digital Image Correlation
EDS	=	Energy-Dispersive Spectroscopy
f	=	frequency
$h(N)$	=	hazard function
$h_0(N)$	=	Cox baseline hazard function
HNBR	=	Hydrogenated Nitrile Butadiene Rubber
$\overline{N_c}$	=	Cox mean fatigue life
$N_c^{\min}$	=	Cox lower 95% bound of fatigue life
$N_c^{\max}$	=	Cox upper 95% bound of fatigue life
N_f	=	fatigue life of a specimen
NBR	=	Nitrile Butadiene Rubber
R	=	loading ratio
$\hat{S}(N)$	=	survival function estimate
T	=	tearing energy (energy release rate)
$\vec{x}$	=	vector of Cox covariates
β	=	Cox regression coefficient
Δt_i	=	duration of cycle i
Δu	=	displacement amplitude
$\Delta\sigma$	=	uniaxial true stress amplitude
$\overline{\Delta\sigma}$	=	average uniaxial true stress amplitude per target loading level
λ	=	stretch ratio
λ_b	=	strain at break
σ	=	uniaxial true stress
$\dot{\bar{\sigma}}$	=	average true stress rate
σ_b	=	stress at break
σ_f	=	fatigue endurance limit

1 Introduction

With increasing economic, safety, and environmental concerns, high performance synthetic elastomers are being extensively adopted across a wide range of industries. Hydrogenated Nitrile Butadiene Rubber (HNBR) is one such synthetic elastomer. It satisfies some of the most important requirements for such materials: compared to other synthetic elastomers, HNBR has high resistance to oil products and other industrial solvents, as well as good aging and heat resistance[1]. Currently, HNBR is mostly used in the automotive industry for production of belts, hoses, vibration dampers, mounts, and seals[2]; it also has found application in aerospace, oil field exploration and processing, military, ship building, and other performance demanding industries[1;3].

HNBR is based on Nitrile Butadiene Rubber (NBR), which is a co-polymer of butadiene and acrylonitrile (ACN), where the double carbon-carbon bonds in the polymer chain are targeted by a selective hydrogenation reaction[4]. Improvement of characteristics over NBR in terms of heat, chemical and environmental resistance, and abrasion is achieved by high saturation level of HNBR[5].

In the present work, the influences of two formulation parameters, acrylonitrile content and percent hydrogenation, are considered.

- The acrylonitrile group, similar as in NBR, functions to provide chemical resistance (to oil and other industrial solvents) and, additionally, provides better strength. It has been reported that, in general, with increasing ACN content: resistance to oil products increases, mechanical performance of HNBR degrades at low temperatures, and glass transition temperature (T_g) roughly increases[2;3;6]. Obrecht *et al.* investigated the effect of ACN content on tensile behavior of HNBR, and found that stiffness increases with ACN content for carbon black (CB) filled HNBR[7].

- The percentage of hydrogenation is defined by the ratio of hydrogenated single bonds to the total quantity of double bonds. Similarly, it has been reported that with increased percent hydrogenation, resistance to heat and to ozone increases[1;6]. With respect to tensile strength, relative stiffness increases and elongation at break decreases for unfilled HNBR from 88 to 92 percent hydrogenation. As compared to NBR (0% hydrogenation), both grades of HNBR are stiffer with significantly higher stress at break[6].

As for fatigue resistance, there are few studies on HNBR, and to the authors' knowledge, there are no published studies on the effects of ACN content and percent hydrogenation on fatigue of HNBR. Kim *et al.* studied fatigue crack propagation behavior, amongst other properties, of HNBR and HNBR/ZDMA blend (with comparison to natural rubber) at room temperature[8]. The investigated materials are HNBR with 44 wt.-% ACN, 91% hydrogenation, and a HNBR/ZDMA blend of Zetpol 2020 (36 wt.-% ACN, 91% hydrogenation) and ZSC 2295 (Zeon Super Composite). Both are carbon black filled at 30 parts per hundred rubber (phr). At room temperature, crack propagation of "pure" HNBR is the fastest followed by natural rubber and the HNBR/ZDMA blend. In another study, Lacroix *et al.* measured fatigue crack propagation of HNBR and polychloroprene (CR) rubbers using a dynamic mechanical analyzer (DMA)[9]. However, the primary objective of the work was not the study of the fatigue behavior of HNBR, but rather the development of a methodology to characterize fatigue crack growth behavior of elastomers. At 80 ˚C, it appears that HNBR has shorter fatigue life as compared to CR for the same testing conditions. Moreover, the size of the initial crack has a greater negative effect on the fatigue life of HNBR. A study on the effect of carbon black fillers on fatigue damage mechanisms of HNBR was carried out by Gauchet[10]. As for other elastomers, the analysis of the fracture surfaces identified three distinct regions: initiation, propagation, and final fracture.

In the present work, an extensive study on the effects of ACN content, percent hydrogenation, and of a composite ACN blend on fatigue resistance of HNBR is carried out. The HNBR blends are chosen with the following criteria: three blends with differing ACN content with constant percent hydrogenation; three blends with differing hydrogenation with constant ACN content; and finally, a composite of two HNBR blends of different ACN content with constant percent hydrogenation. Consequently, fatigue life and fatigue crack propagation experiments are carried out on the six blends and are followed by damage mechanism analysis. Moreover, we utilize a newly adapted, for elastomers, statistical treatment of fatigue life results[11;12]. To closely simulate the real-world operating conditions of HNBR, the testing is carried out on carbon black filled blends of HNBR at a temperature of 120 ˚C.

2 Experimental program

2.1 Material blends and specimen geometry

The formulation of the six blends of HNBR is chosen to closely mimic those used in industrial applications. The detailed formulations are presented in Table 1. HNBR with 36 wt.-% ACN and 96% hydrogenation is thus chosen as a reference, to which other blends are to be compared. The naming convention presented in the table will be used henceforth in the present work. All blends are cross-linked with peroxide and contain 70 phr of carbon black fillers. Additionally, an accelerant, a plasticizer, and two antioxidants (nominally referred to as protectors 1 and 2) are utilised.

Table 1: Formulation of HNBR blends.

Naming convention	**A44H96**	**A36H96**	**A24H96**	**A44-24**	**A36H99**	**A36H91**
	96	96	96	96	>99.5	91
ACN content %	44	36	24	36 average	36	36
	Amount (phr)					
HNBR 44/96	100			60		
HNBR 36/96		100				
HNBR 24/96			100	40		
HNBR 36/99					100	
HNBR 36/91						100
Carbon black (N772)	70	70	70	70	70	70
Plasticizer	5	5	5	5	5	5
MgO	3	3	3	3	3	3
Protector 1	1	1	1	1	1	1
Protector 2	1,5	1,5	1,5	1,5	1,5	1,5
Peroxide	7	7	7	7	7	7

The HNBR blends are compression molded. Two types of specimen are considered as shown in Fig. 1. First, flat dumbbell specimens shown in Fig. 1a are cut using a die for both uniaxial quasistatic tensile and fatigue life testing. Second, 'mini-PS' (PS for pure-shear) specimens are also cut for fatigue crack propagation experiments (see Fig. 1b); this geometry leads to a simple analytical expression of the tearing energy (energy release rate) that does not depend on the length of the crack[13]. It should be noted that both types of specimen do not bear compressive loading due to their thickness; buckling takes place in compression.

2.2 Experimental procedure

The experimental program consists of static tensile characterization, fatigue life and fatigue crack propagation experiments, and macro- and microscopic damage analysis. This follows an approach commonly observed in fatigue studies of elastomers[14;15;16].

2.2.1 Quasi-static uniaxial testing

In order to measure the stress-strain response of materials, uniaxial tensile tests are performed using an electro-mechanical testing machine, Instron 5584. The loading rate is set at 1 mm/s, and the

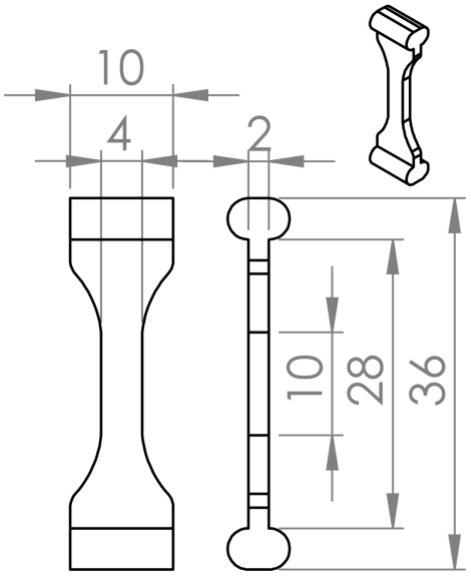

(a) Dumbbell fatigue life specimens.

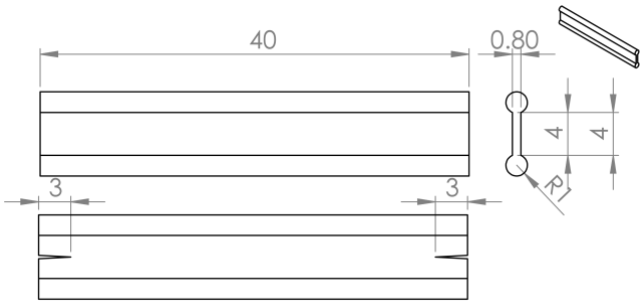

(b) Mini-PS specimens; both notched and un-notched specimens.

Figure 1: Dimensions (in mm) and geometry of specimens.

temperature of a thermal chamber is set to 120 ˚C. Both axial and transverse strain are measured by digital image correlation (DIC). Subsequently, measurement of the force F leads to the true stress

$$\sigma = F/S, \tag{1}$$

where S is the deformed section area, and is calculated due to previously confirmed isotropy and incompressibility of the material. Three specimens are tested for each material.

2.2.2 Fatigue life

Fatigue life experiments are carried out under cyclic loading with constant true stress amplitude

$$\Delta\sigma = \sigma_{max} - \sigma_{min}, \tag{2}$$

and null R-ratio: $R = \sigma_{min}/\sigma_{max} = 0$. The original method used to control true stress throughout the experiments is detailed and extensively discussed in Narynbek Ulu et al.[17] In fact, true stress amplitude loading is a relevant method to compare the fatigue resistance of different blends with different stress-strain responses. The intricacies of the procedure are not recalled here in detail. However, in summary, there are three steps:

1. Two independent investigations are carried out - DIC measurements (axial and transverse) and FE simulations - to calculate the change in cross-section area with respect to the prescribed displacement. Supplementary tests have shown that the tested blends behave in an almost incompressible and isotropic manner, which are the two properties required for application of the method. Then, a machine control algorithm is used to calculate the real time true stress from displacement and force measurements.

2. For each blend and each loading level, two or three specimens are tested individually. It leads to the definition of displacement master curves that contain the evolution of minimum and maximum displacements over a number of cycles, which are required to maintain the target true stress amplitude.

3. The master curves are used to control the loading of eight specimens mounted in parallel with a custom-made system. In this system, each grip is attached to an independent load cell, which permits to monitor the force applied to each specimen.

It should be further noted that this method does not necessitate an accommodation stage for the Mullins effect: it is naturally taken into account through the control of the true stress.

Fatigue life experiments are performed on electrically driven machine, Instron E10000, equipped with a heating chamber. The temperature of the chamber is adapted, depending on loading conditions, to keep the surface temperature of the specimen at 120 °C (measured by a pyrometer). The machine is equipped with a 1 kN load cell. Four target loading levels are considered: 4, 6, 8, and 10 MPa. The average stress rate ($\dot{\bar{\sigma}} = \Delta\sigma/\Delta t_i = f\Delta\sigma$) is set to 20 MPa/s. As mentioned above, the actual true stress applied on each specimen is measured individually, and, on average, at least 8 specimens are tested per blend and loading level.

Due to the plane stress geometry of specimens, the number of cycles to complete failure is considered as the fatigue life, N_f; if a given specimen fails near grips, the corresponding result is discarded. In this experimental setup, several hundred cycles (depending on the loading level) are required by the machine to reach the target stress loading level; this number of cycles is not included in the fatigue life. Initially, the experiments were stopped at 2 million cycles assuming the attainment of the fatigue limit. Additional experiments for the blend A36H96 are carried out until 5 million cycles to improve the statistical estimation of fatigue life distribution.

2.2.3 Statistical analysis of fatigue life results

Generally, scattering is inherent to fatigue life testing of elastomers (and other materials). This is mainly due to material defects introduced during processing and their influence on crack initiation[18]. With the present experimental approach, fatigue life results exhibit the following three characteristics that require to be treated statistically:

- Scattering in fatigue life results;
- Scattering in applied true stress amplitude;
- Presence of unbroken specimens; *i.e.* right-censored data.

In the present work, the Cox proportional hazards model, widely used in medical sciences, is applied on fatigue life data to carry out regression analysis on the results; the details of the statistical approach are discussed in the recently published PhD thesis[11]. Such model can be applied for multivariate analysis taking into account the scatter in both stress amplitude and fatigue life, and presence of right-censored data[19].

In present work, all blends are simultaneously considered. As such, there is one categorical covariate - type of blend (as per model requirements, A36H96 is chosen as the reference). There is also a continuous covariate: the true stress amplitude ($\Delta\sigma$). The hazard function of the Cox model can be formally expressed as

$$h(N,\vec{x}) = h_0(N)\, exp(\beta_{A24H96}x_{A24H96} + \beta_{A36H91}x_{A36H91} + \beta_{A36H91}x_{A36H91} + \beta_{A36H99}x_{A36H99} + \beta_{A44H96}x_{A44H96} + \beta_{A4-424}x_{A44-24} + \beta_{\Delta\sigma}x_{\Delta\sigma}), \quad (3)$$

where N is the fatigue life, $\vec{x}$ is the vector of covariates, $\vec{\beta}$ is the vector of unknown regression coefficients that measure the impact of covariates, and $h_0(N)$ is referred to as the baseline hazard and it corresponds to the hazard when $\vec{x} = 0$. Furthermore, the estimates of the survival function ($\hat{S}$) can be determined, which show the relationship between the probability of survival and number of cycles; hence, one is able to plot the mean fatigue life ($\overline{N_c}$, when $\hat{S} = 5$) and the upper and lower 95% probability bounds ($N_c^{\min}$ and $N_c^{\max}$, when $\hat{S} = 0.05$ and $\hat{S} = 0.95$ respectively). Finally, one can use the model to interpolate and extrapolate the fatigue life results.

2.2.4 Analysis of damage mechanisms

Finally, fracture surfaces of fatigue life specimens are analyzed to identify the initiation site, the nature of possible flaws that are responsible for initiation, and the propagation path. A JEOL JSM6060LA scanning electron microscope (SEM) is used for microscopic analysis. An acceleration voltage of 20 kV, which is chosen due to the conductivity of carbon black filled HNBR blends, is used with capture of secondary electron signal. Depending on the specimen, up to 20 micrographs are taken with magnification ranging from ×20 up to ×5000. Energy-dispersive X-ray spectroscopy (EDS) is applied on selected areas of the fracture surfaces to determine the chemical composition of flaws. The classification and presentation of results is similar to the one used in[20;21].

All fatigue life specimens are analyzed macroscopically with an aid of an optical microscope. For microscopic observations, due to the time-consuming nature of microscopic analysis, only 103 specimens have been analyzed. All specimens of the reference blend A36H96 have been analyzed; for the remaining blends, specimens have been randomly sampled for each of the four loading levels to get a generalized overview of microscopic features.

2.2.5 Fatigue crack propagation

Fatigue crack propagation experiments are performed on MetraVib DMA+300, a specialized DMA testing machine equipped with a stereoscopic microscope and a digital measurement system for monitoring of crack growth rates. The thermal chamber of the DMA machine is set also to 120 ˚C.

Fatigue crack growth rate (*dc/dN*) is plotted with respect to the tearing energy, *T*. The tearing energy for a pure shear specimen (see Fig. 1b) is given by[22;23]

$$T = Wh, \tag{4}$$

where *W* is the strain energy density (per unit of undeformed volume) calculated from integration of the nominal stress vs. stretch ratio pure shear curve performed on an uncracked specimen and *h* is the undeformed height of the specimen. At least six crack growth rate measurements are performed per tearing energy and per blend. Tearing energy varies from 50 to 1000 J/m^2.

Practically, there are four steps in the testing procedure of a given specimen.

- First the material is accommodated for the Mullins effect (stress-softening which depends on the previously endured maximum strain[24]) before energetic characterization of the blends. Additionally, other long-term stress-softening phenomena needs to be taken into account. In this way, the mini-PS specimen is loaded with a simple sinusoidal cyclic loading with a prescribed displacement amplitude of 2.5 mm and R=0 (in terms of displacement). The tearing energy is monitored at each cycle and this accommodation step is stopped after the rate of change of the tearing energy per cycle is less than 1 %, *i.e.* the stress-strain response appears to stabilize. The frequency during the accommodation phase is set to 2.5 Hz.
- The second step consists in the energetic characterization of the specimen as a function of the prescribed displacement amplitude; a condition is set so that at minimum displacement the measured force equals to zero, *i.e* there are no compressive forces or buckling of the specimen. The amplitude is increased in equal increments from 0.2 mm to 2 mm and the tearing energy is calculated after 150 cycles. The frequency is set to 2.5 Hz. Subsequently, the relationship between the prescribed displacement amplitude and the tearing energy is established and can be closely fitted by a power law

  $$T = A(\Delta u)^C, \tag{5}$$

  where A and C are scalar constants, and Δu is the displacement amplitude.
- The third step entails introducing, *in-situ*, 2 notches of 3 mm at a vertical midpoint at both ends of a specimen as shown in Fig. 1b.
- Finally, a displacement amplitude for a specific tearing energy applied and fatigue crack growth rate is recorded after a given number of cycles. To reduce the duration of experiments, the frequency of 24.5 Hz is chosen; preliminary tests showed that there is no significant effect of frequency (2.5, 10.0, and 24.5 Hz) on the measured crack growth rate.

  Results are plotted on a traditional *dc/dN* vs. *T* curves, where *T* is the maximum prescribed tearing energy. Subsequently, a power law relationship is calculated from multiple linear regression

$$\frac{dc}{dN} = bT^f, \tag{6}$$

where *b* and *f* are fitted scalars.

Due to the nature of fatigue crack-tip blunting after the initial introduction of a notch[25;26;27], stabilization of the crack growth rate is observed after several cycles and this value is recorded. For relatively high tearing energies, where crack growth rate is large, the interval between the measurements is relatively short and crack propagation distances are long; thus, the specimen is discarded after one crack growth rate measurement. Otherwise, the crack growth rate is measured for one specific tearing energy (after its stabilization) and measurements are continued on the same specimen with decreasing tearing energy.

3 Results

3.1 Quasi-static uniaxial testing

Fig. 2 shows the average stress-strain response of all blends within the stress range used in fatigue life testing (4 to 10 MPa). With respect to ACN content, the general stiffness of A44H96 and

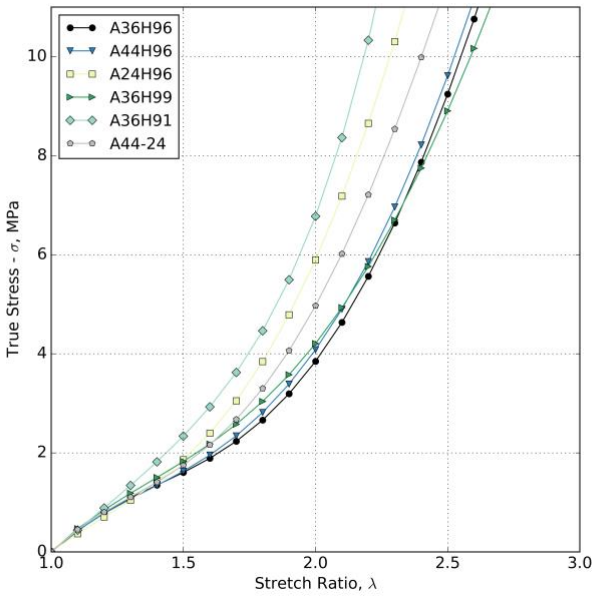

Figure 2: Average stress-strain responses of all tested blends at 120 °C within stress range of fatigue life experiments.

A36H96 are similar. However, that of A24H96 is higher and, thus, this blend has a more 'brittle' response. The trend is similar for increasing percent hydrogenation. A36H91 also has more 'brittle' response with a higher stiffness modulus (and small stress and strain at break). HNBR with 96% and 99% hydrogenation have similar stiffness up to 10 MPa. Moreover, A44-24 blend of HNBR is stiffer than that with 36 wt.-% ACN and softer than that with 24 wt.-%.

For overall stress-strain behavior, both stress and strain at break are shown in Table 2 (full curves are available as supporting information). The indices and superscripts indicate the variance in measured stress and strain at break. As the ACN content increases from 24 wt.-% to 36 wt.-% and

Table 2: Stress and strain at break of the six HNBR blends at 120 ◦ C.

Blend	λ_b		σ_b (MPa)	
A36H96	3.29	$^{+0.09}_{-0.06}$	23.84	$^{+1.25}_{-0.92}$
A44H96	3.92	$^{+0.15}_{-0.18}$	38.47	$^{+2.07}_{-1.68}$
A24H96	2.41	$^{+0.07}_{-0.06}$	12.37	$^{+0.73}_{-0.37}$
A36H99	3.60	$^{+0.09}_{-0.11}$	25.96	$^{+0.42}_{-0.49}$
A36H91	2.37	$^{+0.11}_{-0.07}$	14.76	$^{+0.49}_{-1.56}$
A44-24	2.85	$^{+0.05}_{-0.06}$	17.29	$^{+0.64}_{-0.69}$

to 44 wt.-%, there is a significant increase in stress (from σ_b=12.4 to 23.8 to 38.5 MPa) and strain (from λ_b=2.4 to 3.3 to 3.9) at break. Similarly, there is an increase in stress (from σ_b=14.8 to 23.8 to 26.0 MPa) and strain (from λ_b=2.4 to 3.3 to 3.6) at break with an increase of hydrogenation from 91% to 96% and to 99%, respectively. As for the composite HNBR of 24 wt.-% and 44 wt.-% ACN (average of 36 wt.-%), it appears to have an intermediate stress (σ_b=17.3 MPa) and strain (λ_b=2.9) at break as compared to the original blends.

3.2 Fatigue life

Fig. 3 presents Wöhler curves of the different blends: Fig. 3a shows the effect of ACN content, Fig. 3b focuses on the effect of hydrogenation, and Fig. 3c highlights the fatigue life of the composite HNBR with 24 wt.-% and 44 wt.-% ACN. In fact, the applied stress amplitude is never truly constant, each value on the y-axis represents the average stress amplitude over the fatigue lifetime; the error bars (where visible) indicate the absolute maximum and minimum stress amplitudes measured for each specimen. At the lowest target level of 4 MPa, there are unbroken specimens as indicated in the legends. It should be noted that there is scattering in both *x*- and *y*- axes: it is relatively small around each stress amplitude level and more significant in fatigue life measurements.

For statistical analysis, the Cox proportional hazards model is applied on the data presented in Figs. 3a-3c. As an example of the results of Cox analysis, Fig. 4 shows a probabilistic Wöhler curve for the reference blend A36H96. Here, the solid lines indicate the mean probability, as well as near absolute survival and near absolute failure (as indicated by labels $\hat{S}$ =0.500, $\hat{S}$ =0.999, and $\hat{S}$ =0.001). The dashed regions from 2 to 4 MPa and from 10 to 12 MPa indicate the extrapolated regions.

To aid with the comparison of the blends, the mean lines are compared for each formulation category. Fig. 5 shows the results, where solid lines indicate the Cox mean ($\overline{N_c}$) and dotted lines represent the extrapolated values also obtained from the Cox regression of Eq.(3). First, Fig. 5a shows the effects of ACN content. In general, A36H96 has the best fatigue resistance at 120 °C followed by A44H96; however, from about 8.6 MPa and larger, A44H96 has slightly longer fatigue lives than A36H96. On the other hand, A24H96 evidently has shorter fatigue lives as compared to the two other blends. Second, the effects of hydrogenation are shown in Fig. 5b. In this case, the difference between fatigue lives is less pronounced than for ACN content. Moreover, it is evident that A36H96 has in general longer mean fatigue lives, except, again, from about 8.3 MPa and larger, where A36H99 has a slightly longer fatigue life. On the other hand, A36H91 has consistently lower mean fatigue lives. Finally, Fig. 5c presents the fatigue life of composite A44-24 with comparison to the reference A36H96; fatigue life of the composite A44-24 is significantly shorter than that of the reference A36H96.

3.3 Damage mechanism analysis

3.3.1 Macroscopic observations

First, the general nature of crack growth within the specimens has been investigated. For all tested specimens, this behavior can be split into two categories (corresponding schematic is available as supporting information):

- When initiation and propagation occur on a single plane perpendicular to the direction of loading;

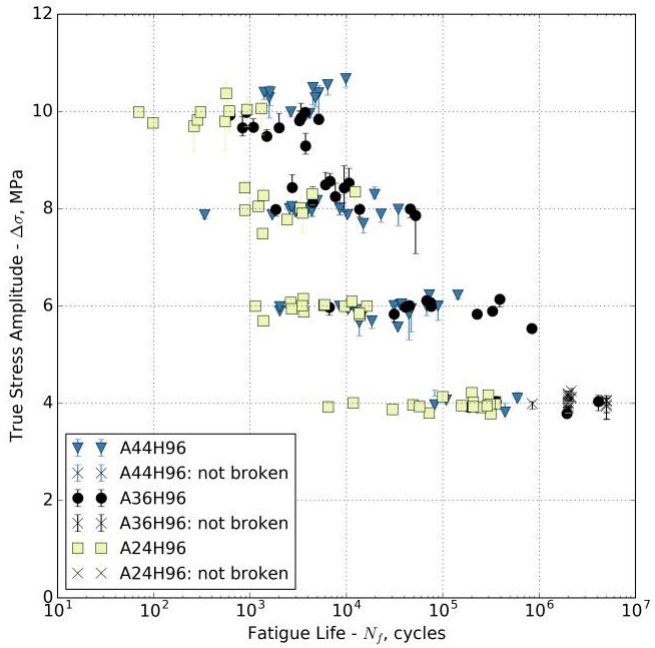

(a) Effect of ACN content.

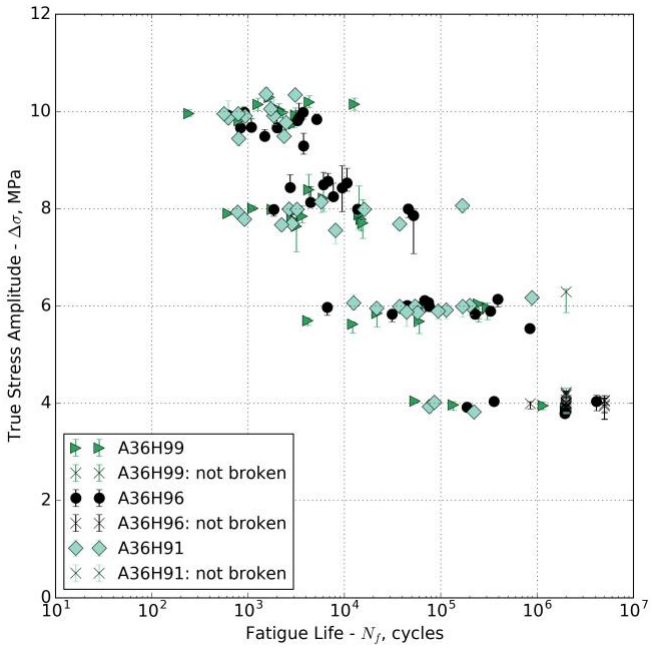

(b) Effect of hydrogenation.

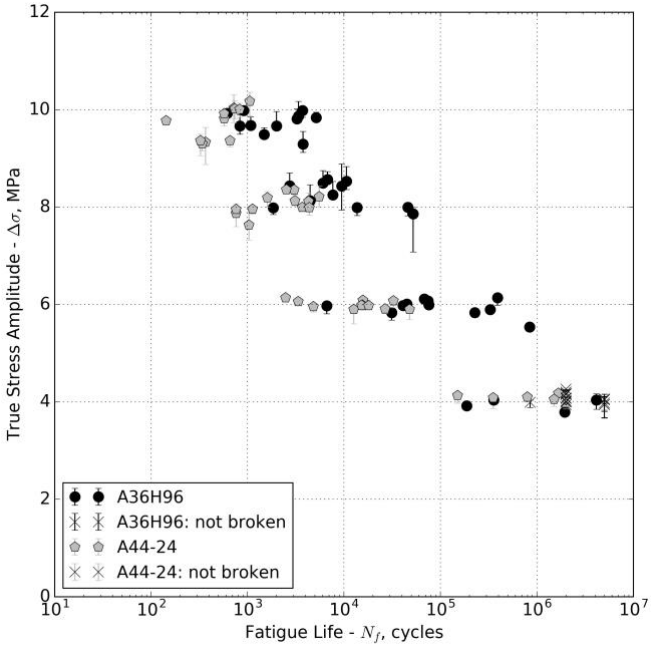

(c) Fatigue life of composite A44-24.

Figure 3: Fatigue life of HNBR at 120 °C and R=0; effect of ACN content, percent hydrogenation, and for composite A44-24. Crosses indicate unbroken specimens.

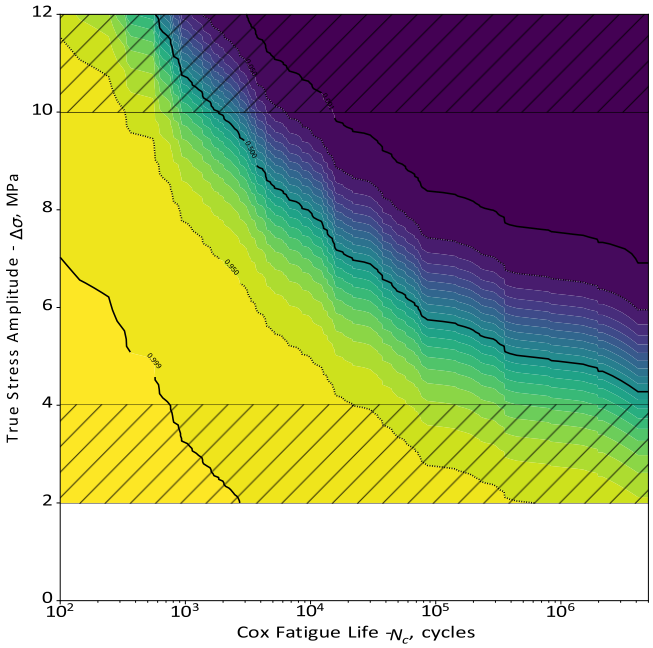

Figure 4: Probabilistic Wo¨hler curve of A36H96 obtained from Cox analysis.

- When initiation occurs on “plane 1” and brittle, smooth failure surface is observed on “plane 2” that is offset by some vertical distance (along the direction of loading).

Furthermore, measurements are made along the specimen length to record the vertical length of crack propagation, L_P, *i.e.* the distance between two planes. Finally, observations have been made to detect any signs of multiple cracks present on both failed and unbroken specimens after fatigue life testing.

The observations of the nature of crack growth (on a plane or two planes), vertical length of crack propagation, and the presence of multi-cracking in failed specimens are summarized in Fig. 6. A trend is clear from Fig. 6: the six blends can be divided into two groups.

- A36H96, A44H96, and A36H99 are blends with longer vertical propagation lengths spanning in some cases two planes, and presence of some multi-cracking.

  The greatest number of failed specimens have vertical propagation lengths from 5% to 15% for A36H96 and A44H96 and from 2% to 15% for A36H99. All three blends also have some specimens breaking up to 30%. Moreover, vertical propagation lengths greater than 30% have been observed for blends A36H96 and A44H96. Thus, these blends have two macroscopic crack growth mechanisms. In some specimens (38% for A36H96, 55% for A44H96, 80% for A36H99), crack initiates on one plane and crack grows in the same plane, which is perpendicular to the loading direction. However, for the remaining failed specimens, crack growth behavior is best described by initiation on one plane, followed by vertical crack growth along the length of a specimen, and final failure on a second plane. Finally, multi-cracking is observed in some of the specimens with largest frequency in A36H96 (12%), followed by A44H96 (7%), and A36H99 (4%).

- A36H91, A24H96, and A44-24 are blends with short vertical propagation lengths with crack growth occurring on one plane, and absence of multi-cracking.

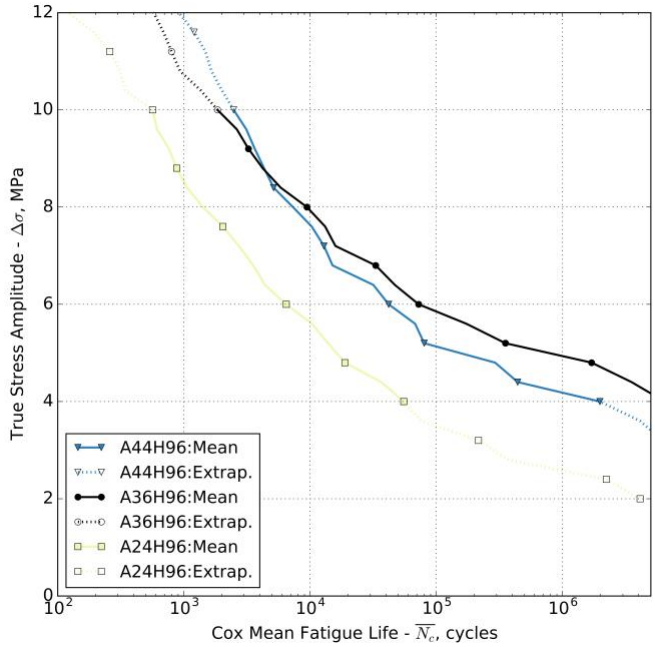

(a) ACN content.

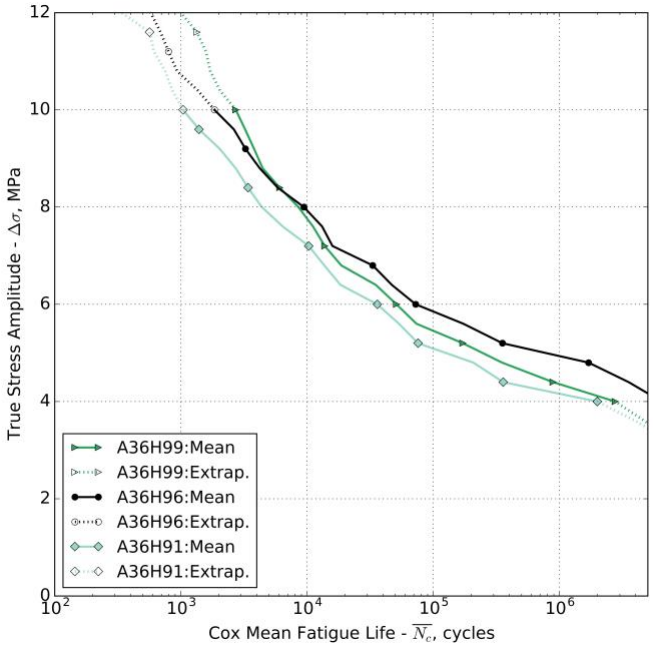

(b) Percent hydrogenation.

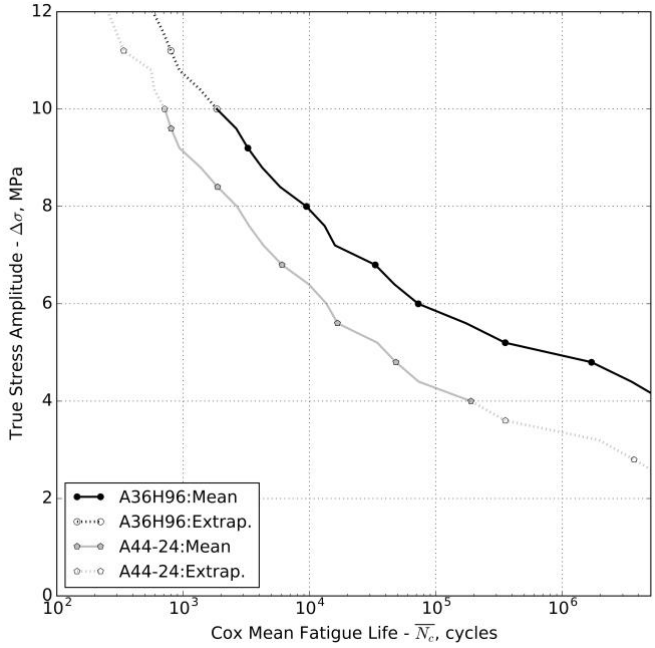

(c) Composite A44-24.

Figure 5: Mean fatigue lives of the Cox model ($\overline{N_c}$); effect of ACN content, percent hydrogenation, and for composite A44-24.

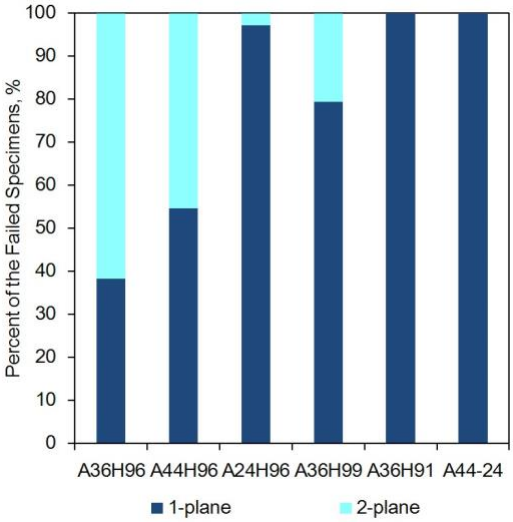

(a) Crack growth behavior.

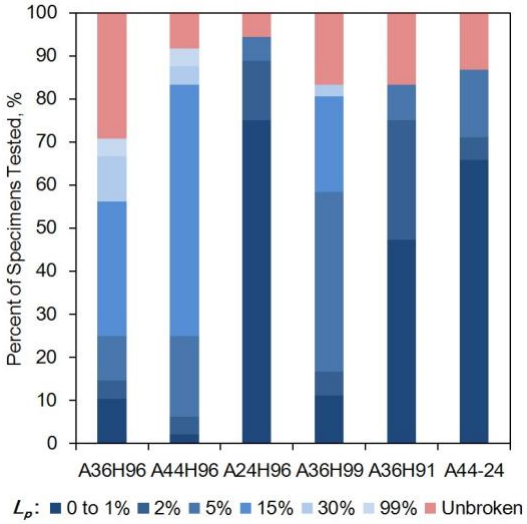

(b) Vertical length of propagation (L_P).

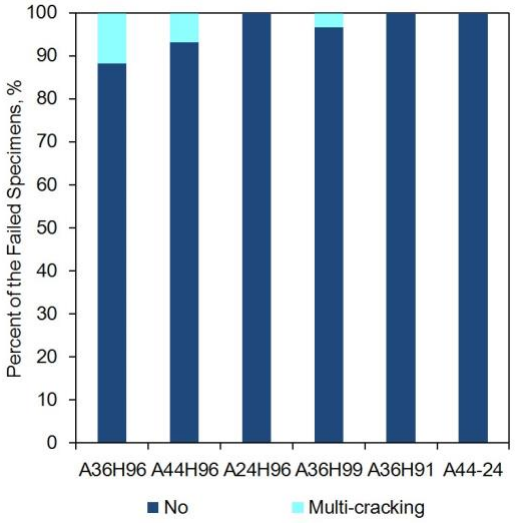

(c) Multi-crack appearance.

Figure 6: Macroscopic observations of crack growth behavior, vertical length of crack propagation, and of appearance of multi-cracking in broken specimens.

In this case, vertical crack propagation lengths are less than 2% of the total specimen length for the vast majority of specimens. In none of the specimens, the vertical propagation lengths are greater than 5%. Thus, the macroscopic crack growth mechanism of these blends is simple initiation, growth, and failure on one plane perpendicular to the loading direction. Finally, no multi-cracking occurs in these blends.

These results are compelling since, if one recalls the results of the previous sections, the blends in the group with long vertical propagation lengths had generally better resistance to fatigue (long lives, slow propagation) than the blends of the group with short vertical lengths.

3.3.2 Microscopic observations

In general, the fracture surfaces can be categorized into three categories (corresponding micrographs are available as supporting information):

1. Classic surfaces with three regimes of initiation, propagation with high rugosity (roughness), and failure with low rugosity (smoothness); these are related to one-plane macroscopic observations and will be referred to as *rough-smooth*;
2. Similar surfaces except with the earlier mentioned vertical propagation; these are related to two-plane macroscopic observations and will be referred to as *vertical rough-smooth*;
3. Finally, almost completely smooth surfaces over the whole fracture surface of a specimen; these are related to one-plane macroscopic observations and will be referred to as *smooth*.

The number of observations for each category of fracture surfaces is shown in Fig. 7; it should be

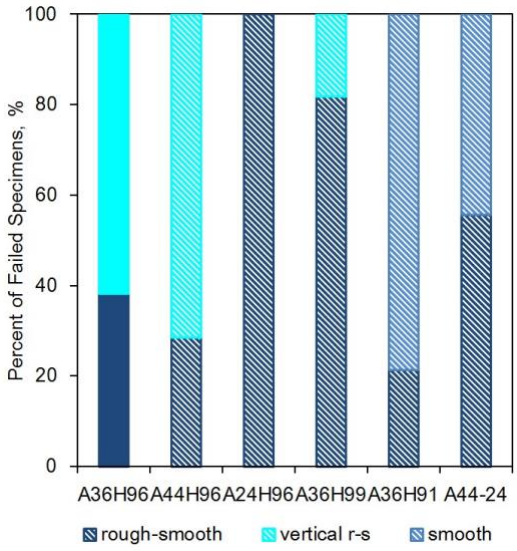

Figure 7: Microscopic observations of fracture surfaces categories in broken specimens; hatched fill indicates partial sampling.

noted that partial random sampling is done for all blends except for A36H96 (for which all specimens have been observed) and, as such, are indicated by hatched fill. The results are very similar to those presented in Fig. 6 and a parallel can be drawn that separates the materials into two groups: on one hand, A36H96, A44H96, and A36H99 with both *rough-smooth* and *vertical rough-smooth* fracture surfaces; on the other hand - A24H96, A36H91, and A44-24 with *rough-smooth* and *smooth* fracture surfaces.

Of special interest are the *vertical rough-smooth* fracture surfaces, and example of which is shown in Fig. 8. The initiation site is shown in Fig. 8a, where the arrow points to a flaw on the surface of the specimen. One can observe the initial propagation in a semi-circular fashion with the so-called "fatigue rivers" radiating away from the initiation site. Subsequently, the propagation path is shown in Fig. 8b. The circular region is the initiation site from Fig. 8a, and the white arrows indicate the initial propagation within a plane away from the initiation site. Afterwards, the crack propagates in the vertical direction, as indicated by red lines. Finally, there is a rapid fracture as indicated by the smooth surface in Fig. 8c.

It is interesting to observe the "side" of a specimen that has *vertical rough-smooth* surface, as technically these also make up the fracture surface. Fig. 9 shows such view of an A36H96 specimen tested at 6 MPa. The arrows indicate presence of some flaws such as embedded particles or voids (it is unclear whether these are due to missing particles or material voids). Similar results have been observed for other specimens, which failed in such manner. Without possibility for additional

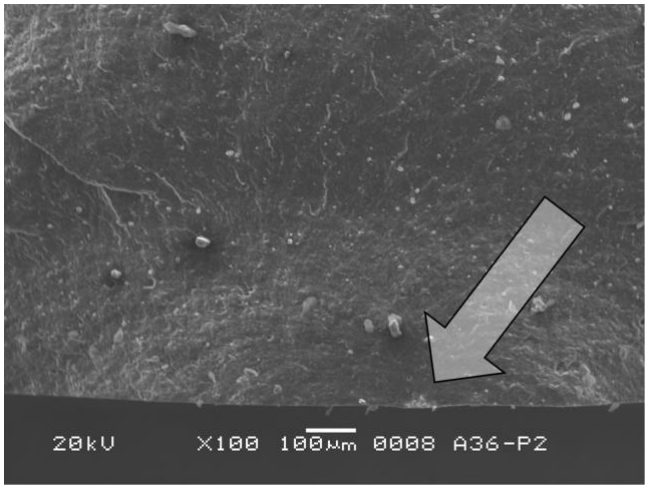

(a) Initiation site at ×100.

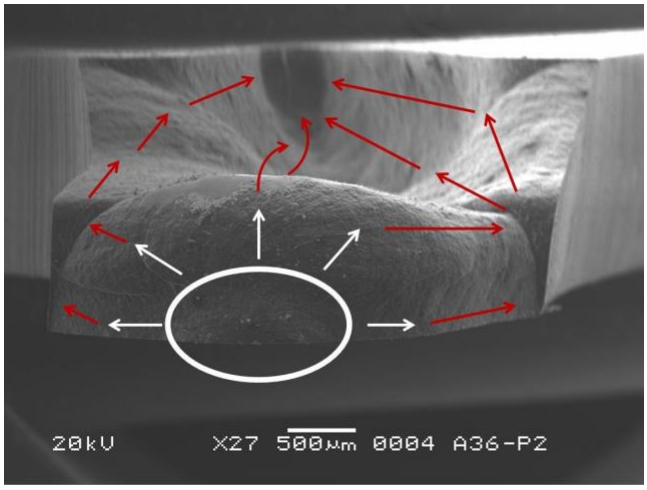

(b) Propagation path ×27.

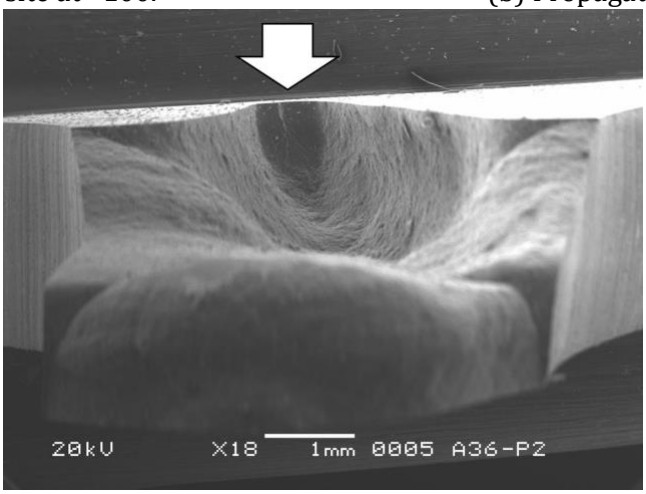

(c) Final fracture ×18.

Figure 8: Micrograph with an example of a *vertical rough-smooth* fracture surface; A36H96 specimen tested at 4 MPa target loading level.

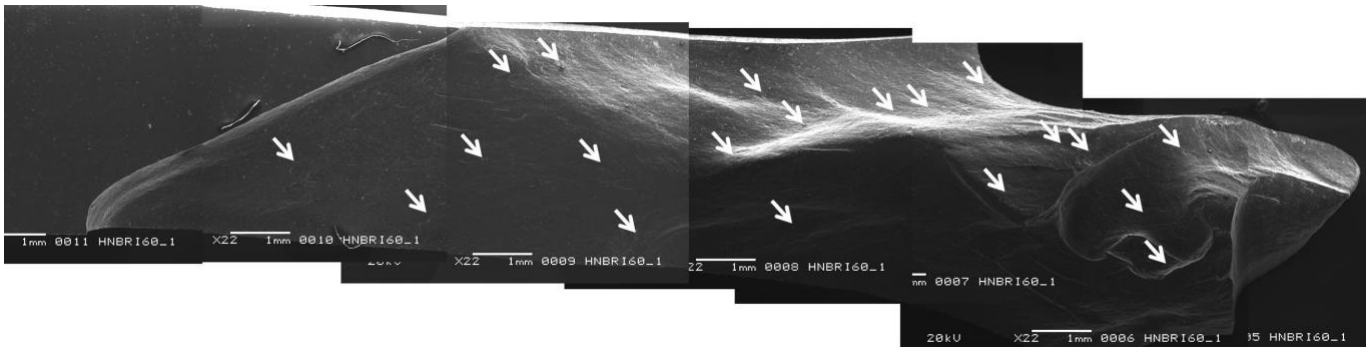

Figure 9: "Side" composite micrograph of a *vertical rough-smooth* fracture surface; A36H96 tested at 6 MPa.

interrupted testing or use of other tools such as micro CT, only a hypothetical damage mechanism for such failures can be proposed.

1. A crack initiates due to a critical flaw in the specimen. In the meantime, other smaller cracks initiate within the specimen.
2. The critical flaw grows by following a stress path of "least resistance," leading to coalescence and absorption of smaller cracks. Thus, the propagation occurs not strictly on a plane.
3. The crack reaches a critical size and there is a sudden, rapid failure.

3.3.3 Causes of fatigue crack initiation

The initiation sites have been analyzed with energy-dispersive X-ray spectroscopy (EDS). All initiation sites of the reference blend A36H96 have been analyzed; as mentioned earlier, for the other five blends, random sampling has been used to get a general idea and to investigate whether it differed from those of A36H96 and no trends have been observed by comparing the types and the frequency of inclusions found in each blend. In many cases, an initiation site can be clearly observed, but EDS analysis did not exhibit any differences with respect to the matrix chemical composition; in other cases, six different elements/particles have been detected. All seven can be grouped into the following: matrix (no difference); voids; oxides; carbon black; large contaminants (fibers, *etc.*); metals; ZnO. Flaws such as oxides, large particles, metals, and ZnO are mostly likely introduced during manufacturing. By comparing EDS spectra specific to these inclusions to a spectrum of the matrix, it can be said that none of these appear to be used in the formulation.

Fig. 10a shows the frequency of occurrence of these types of flaws in all observed specimens. The largest number of initiations are caused by an unknown/undetected particle or material heterogeneity (matrix). Out of the identified flaws, presence of oxides causes most initiations (31%). This is followed by initiation due to carbon black agglomerates (10%). Large particles, such as fibers, make up about 9% of flaws. Metal and ZnO particles and voids initiate about 4% each. On the other hand, Fig. 10b shows the percentages for each blend; note that hatched fill indicates that not all specimens have been observed for all blends except for A36H96. Thus, it is hard to draw concrete conclusions on whether certain flaws are more frequent in one blend or another. Finally, an attempt has been made to find a relationship between fatigue life and the type of initiations, but no correlation has been observed.

Furthermore, the location of these flaws is shown for all specimens in Fig. 11. Fig. 11a shows the coordinate system used to record the location of the initiation sites, where the cross-section area of a specimen is divided into quadrants and all sites are recorded with respect to one quadrant due to the 2-axis symmetry of the specimen. Fig. 11b shows the distribution of the sites as a percentage of all observed sites. If one recalls from earlier, the specimens have been compression molded into sheets and then cut with a die. Correspondingly, first, we can categorize surface cracks:

- About 17% of initiation sites occur on the long surface (along the *x*-axis) that corresponds to the molded surface. EDS analysis of the initiation sites showed presence of various flaws: oxides, ZnO, metal, and large contaminants. About a third is categorized as matrix since EDS analysis did not show differentiation with respect to the matrix. However, it seems likely that these flaws are result of contaminants present on the mold surface.

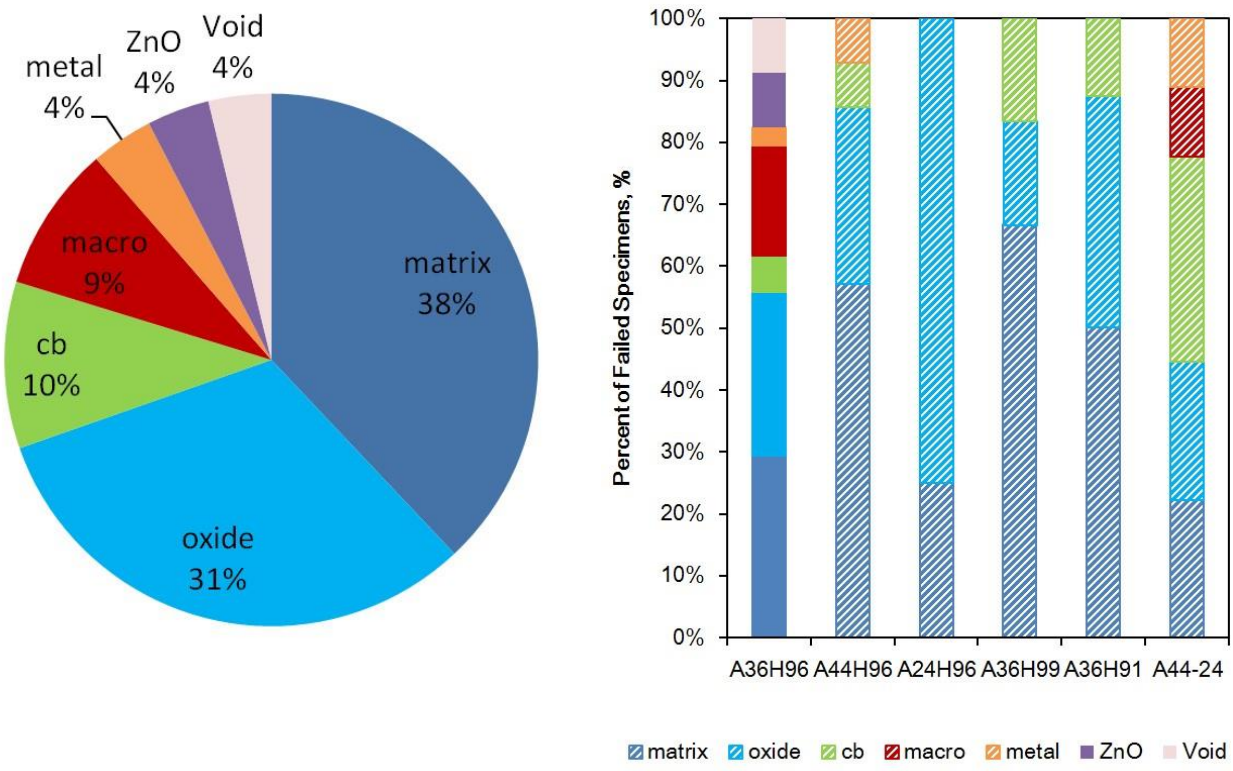

(a) All blends. (b) For each blend.

Figure 10: Different causes of fatigue initiation in analyzed specimens; hatched fill indicates partial sampling.

- On the other hand, 9% of initiations formed on the short surface (along the *y*-axis) corresponding to the surfaces created by a cutting die. For these, all except one are flaws of matrix type; hence, it seems that the initiation site is caused by rough surface created from cutting. The other is due to presence of carbon black. This includes about 1% of initiation sites that occur in the corner of the specimen; for these, all flaw types are categorized as matrix (similarly EDS showed no differentiation). Thus, these are also mostly likely caused by some initial damage

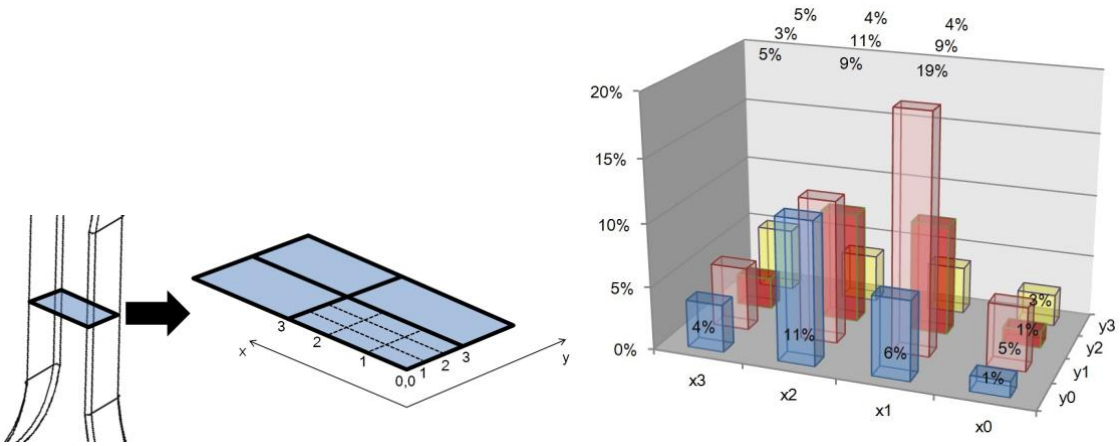

(a) Coordinate scheme. (b) Distribution per location in %.

Figure 11: Initiation site location in all observed specimens.

due to cutting.

The remaining initiation sites (majority) are located inside the specimen; all types of flaws are present. With respect to foreign particles, it appears that these are also introduced during mixing in addition to contamination during molding.

3.4 Fatigue crack propagation

Fatigue crack propagation results are shown in Fig. 12; data fitted power law coefficients are shown in Table 3.

Table 3: Power law coefficients characterizing fatigue crack propagation: effect of ACN content, percent hydrogenation, and for composite A44-24.

	A36H96	**A44H96**	**A24H96**	**A36H99**	**A36H91**	**A44-24**
b	8.53E-10	1.96E-09	2.43E-07	9.91E-08	9.93E-07	4.13E-06
f	4.09	3.92	3.59	3.43	3.41	3.06

Referring to Fig. 12a showing the effect of ACN content on fatigue crack propagation, A36H96 and A44H96 generally have similar resistance to fatigue crack growth. This is confirmed by fitted coefficients given in Table 3. A decrease in ACN content to 24 wt.-%, significantly increases fatigue crack growth rates. With the data available, it is difficult to judge whether there are distinct propagation regimes as originally proposed in Lake and Lindley[28]. However, it seems that around $T \approx 100$ J/m^2 there is a transition in regimes for A44H96 and A36H96, where the "slope" (or *f*) increases with greater tearing energy. Hence, for consistency, the power-law fit only considers points above this tearing energy.

At low energies ($T < 100$ J/m^2), cracks propagate faster in A44H96 (≈ 0.6 nm/cycle) than in A36H96 (≈ 0.1 nm/cycle). Indeed, it seems that these low energy crack growth measurements point to existence of some value that corresponds to only the environmental effect (in present case temperature)[27]. Without direct measurements, it could be estimated that for these two blends the mechanical fatigue threshold T_0 is around 50 to 100 J/m^2. In case of A24H96, there is no apparent change in "slope" such that a regime transition occurs. At tearing energies equal to and higher than ≈ 600 J/m^2 (indicated by dashed line in Fig. 12a), complete failure occurs during the first loading cycle.

Keeping the reference blend A36H96, the fatigue crack propagation results with respect to changing percent hydrogenation are shown in Fig. 12b. Once again, in two blends, A36H99 and A36H96, two regimes are observed with a transition roughly around $T = 100$ J/m^2, and, for consistency, a power-law fit is plotted for energies greater than $T = 100$ J/m^2 with coefficients given in Table 3. The reference HNBR blend with 96% hydrogenation has generally better resistance to fatigue crack propagation. At the lowest energies around 50 J/m^2, there is some overlap in crack growth rate measurements of blends with 99% and 96% hydrogenation. Moreover, there appears to be no drastic transition in the regime (change of "slope" *f*) in A36H99, which could indicate smaller fatigue threshold values for A36H99 than for A36H96, or that such threshold does not exist for A36H99. Additionally, propagation is similar for energies higher than 1000 J/m^2. Whereas the difference between A36H96 and A36H99 is relatively insignificant, resistance to fatigue crack growth is greatly

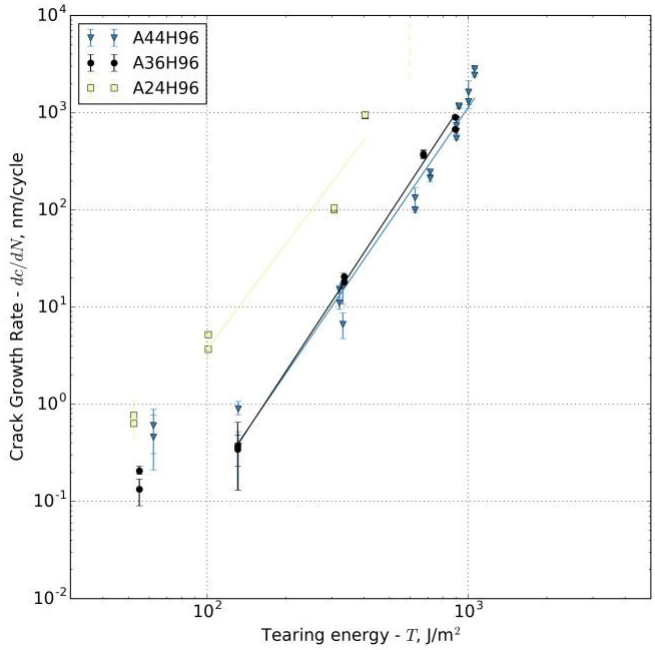

(a) Effect of ACN content.

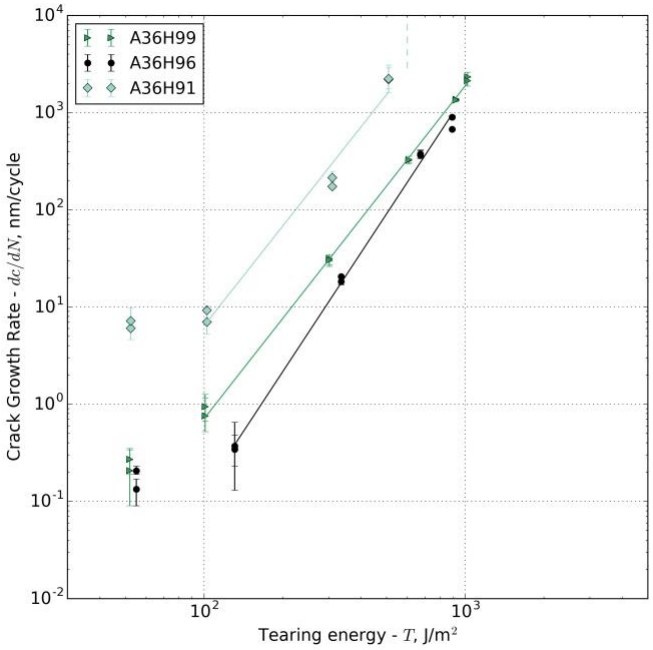

(b) Effect of hydrogenation.

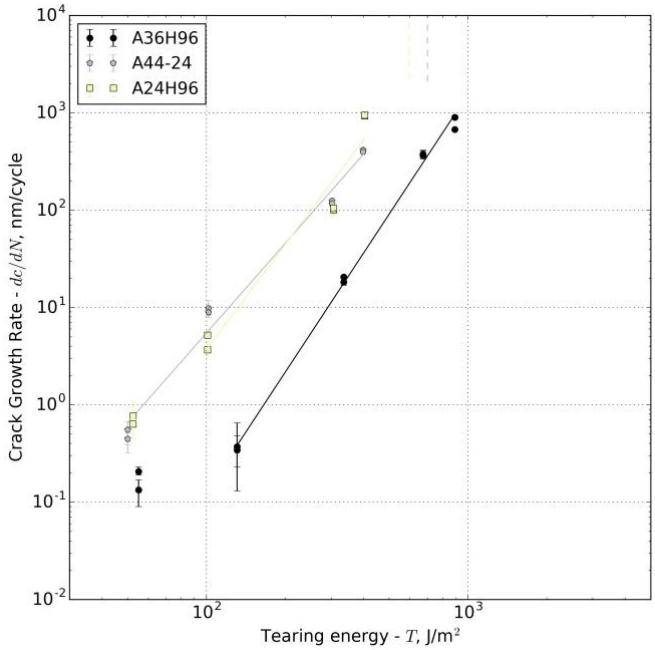

(c) Composite A44-24.

Figure 12: Fatigue crack propagation of HNBR at 120 °C and R=0; effect of ACN content, percent hydrogenation, and for composite A44-24.

diminished as percent hydrogenation is reduced to 91%: at low energies around 50 J/m^2, where environmental contribution is significant, the growth rate for A36H91 is around 7 nm/cycle and decreases to around 0.2 nm/cycle for the other two blends. At the other extreme of tearing energies, A36H91 (similar to A24H96) has a critical tearing energy T_c since it suffered instantaneous failure at tearing energies equaling and greater than ≈ 600 J/m^2, as indicated by dashed line in Fig. 12b.

Finally, Fig. 12c and coefficients in Table 3 show that fatigue crack propagation resistance of the composite HNBR is similar to the blend with 24 wt.-% ACN, the resistance of which is significantly lower than the one of the reference blend, A36H96. Moreover, similar to A36H91 and A24H96, cyclic loading at tearing energies of about 700 J/m^2 and higher could not be applied due to failure of the specimens, thus indicating the existence of critical tearing energy T_c.

4 Discussion

4.1 Effect of Acrylonitrile Content

The three experimental approaches lead to similar general conclusions on the effect of ACN on fatigue resistance of HNBR at 120 °C: A36H96 has better fatigue resistance, followed by A44H96, and A24H96 has significantly less resistance to fatigue as compared to the other two blends.

First, this is supported by fatigue life experiments as shown in Fig. 5a. Second, fatigue damage analysis in both macroscopic and microscopic scales exhibits a trend, where all blends can be grouped in two categories: A36H96 and A44H96 in one, and A24H96 in the other. Macroscopic observations have shown that A44H96 and A36H96 (to a greater extent) have a significant number of cracks growing along the loading direction, whereas crack growth in A24H96 occurs on a single plane perpendicular to the loading direction. These results are analogous to the microscopic observations of fracture surfaces. In A36H96 and A44H96, there are classic initiation-propagation-failure regimes on a single plane perpendicular to the direction of loading. However, there are also similar type of failures that have propagation regime occurring in the vertical direction corresponding to macroscopic observations. However, the propagation regimes of A24H96 take place on a single plane. Finally, macroscopic multi-cracking can be observed in about 12% of failed A36H96 specimens and in A44H96 specimens to a lesser extent, but this phenomenon is completely absent in A24H96 specimens.

Third, fatigue crack propagation experiments show similar growth rates for both A36H96 and A44H96; on the other hand, A24H96 has crack growth rates on an order of magnitude higher for same tearing energies; the results are shown in Fig. 12a.

On the other hand, it is also of interest to speculate on the connections between the three experimental approaches. At first glance, it appears that occurrence of crack growth in direction parallel to loading could be an indication of good resistance to fatigue crack propagation. Since in all three blends cracks initiate from flaws, it could be argued that longer fatigue lives are a result of slow crack propagation rates. However, this explanation is not all satisfactory because fatigue life specimens are thin, with the implication being that the crack propagation phase of fatigue life is negligible as compared to the initiation phase; moreover, this is not sufficient to explain the difference in fatigue lives for different stress loading for blends A36H96 and A44H96. Perhaps, the difference between these blends (especially between A36H96/A44H96 and A24H96) can be discussed by determining the fatigue endurance limit (σ_f) to the stress at break, as it is usually done for metals (e.g. Stephens et al.[29]). Here, the fatigue ratio (0.5 in steels for example[29]), which can be said to represent the efficiency of a material in fatigue, can be introduced

$$\mathrm{FR} = \frac{\sigma_f}{\sigma_b}, \tag{7}$$

where the fatigue endurance limit σ_f is chosen as the corresponding true stress amplitude for the Cox mean fatigue life at 2 million cycles.

The fatigue ratios are around 0.2 for both A36H96 and A24H96, and around 0.1 for A44H96. In fact, if one considers efficiency of each material in fatigue, A36H96 and A24H96 are identical, and A44H96 is almost twice less as efficient. Thus, relatively poor fatigue life performance of A24H96 is simply due to its mechanical weakness as shown in tensile test results: its stress at break is roughly 12 MPa, which is very close to the maximum loading level of 10 MPa applied in this study. Finally, it

should be mentioned that HNBR blends with low ACN content are mostly designed to be used at low temperatures (they admit low T_g) and, it appears obvious that use of A24H96 for applications at 120 ˚C is not a good choice if good fatigue resistance is required.

On the other hand, the fatigue ratio does not explain the difference between A36H96 and A44H96. In terms of applied loading, A44H96 has almost twice the stress at break than A36H96 (38.5 MPa vs. 23.8 MPa). If one recalls Fig. 5a, A44H96 has and is extrapolated to have longer fatigue lives from around 8.5 MPa and greater; perhaps the load range from 4 to 8.5 MPa, thus, does not have significant influence on fatigue life. Thus, it seems that in fatigue applications, where high loading is expected (on average or with "peak" loads) at 120 °C, A44H96 is a good choice.

In terms of damage mechanics, A36H96 did exhibit more frequently the more "favorable" damage mechanism with greater occurrence of vertical cracks and observation of multi-cracking; one could assume that such phenomenon allows for dissipation of energy and delay of fracture. Perhaps A36H96 has a higher fatigue propagation threshold and, consequently, better resistance to initiation/propagation transition of existing flaws; however, a deeper investigation is required to fully answer this question. Nonetheless, it is obvious that A36H96 is the best choice for general fatigue applications at 120 °C.

4.2 Effect of Hydrogenation

Similar to the results on the effect of acrylonitrile, but with less pronounced differences, the results of the effect of hydrogenation from the three experimental approaches are also in accordance with each other: A36H96 has better fatigue resistance, followed by A36H99, and followed by A36H91. In the discussion of the results, a parallel can be drawn:

- Fatigue life experiments and subsequent statistical analysis show that A36H96 has longer fatigue life, followed by A36H99, and A36H91; the results are shown in Fig. 5b.

- Fatigue crack propagation experiments show that A36H96 has better resistance to fatigue than A36H99 (although these appear similar at very high tearing energies); on the other hand, A36H91 has crack growth rates on an order of magnitude larger for same tearing energies; the results are shown in Fig. 12b.

- Fatigue damage analysis is similar in both macroscopic and microscopic scales and, once again, the blends can be grouped in two categories: A36H96 and A36H99 in one, and A36H91 in the other.

  Macroscopic observations have shown that A36H96, to a greater extent, and A36H99 have numerous cracks growing along the direction of loading; A36H91, similar to A24H96, has cracks occurring on a single plane perpendicular to the direction of loading.

  Likewise, most fracture surfaces of A36H96 and A36H99 present classic initiation-propagation failure regimes on a single plane perpendicular to the direction of loading; but, once again, there are fracture surfaces that have propagation occurring in the vertical direction corresponding to the macroscopic observations. Such phenomenon was not observed for A36H91 and, moreover, some completely smooth fracture surfaces have been observed, which are similar to those of quasi-static tensile failure. Finally, in about 12% of failed A36H96

specimens multi-cracking can be observed and in about 4% of A36H99 specimens, but this phenomenon is completely absent in A36H91 specimens.

Recall that the fatigue ratio of the reference blend is around 0.2; A36H91 has higher efficiency in fatigue with a ratio of around 0.27, even though it has the lowest mean fatigue lives of the three blends, while A36H99 has the lowest efficiency with a ratio of 0.16.

Starting with A36H91, the results discussed above show that at 120 °C fatigue resistance of A36H91 is worse than of A36H96 and A36H99. It seems likely that A36H91 is not an optimal material in fatigue resistance at 120 ° C, even though it has high fatigue efficiency relative to its ultimate stress. As for A36H99, it can be argued that this is a surprising result, considering that heat resistance increases with percent hydrogenation: thus, it would be expected to have an increase in fatigue efficiency with percent hydrogenation for fatigue tests carried out at 120 °C. Perhaps the expected better resistance is not sufficiently accounted for tests at 120 °C. It seems likely that fatigue testing at higher temperatures, taking into account that the general application limit is around 150 °C, could show that it has better fatigue performance than A36H96. This is an interesting result and a study on the influence of temperature is planned for the near future. Nonetheless, for practical applications at 120 °C, where relatively high strength and fatigue resistance are required, A36H96 is once again the better choice.

4.3 Fatigue resistance of the composite blend - A44-24

Once again, three experimental approaches come to the same conclusion: composite A44-24, with average ACN content of 36%, has significantly lower fatigue resistance than A36H96.

- Fatigue life experiments and statistical analysis show that composite A44-24 has significantly shorter fatigue life than the reference A36H96 as shown in Fig. 5c.

- Fatigue crack propagation experiments show that A44-24 has significantly larger crack growth rates than A36H96; moreover, they seem to closely match the results obtained for A24H96. The results are shown in Fig. 12c.

- Fatigue damage observed in A44-24 significantly differs from that in A36H96 and seems similar to the one observed in A24H96. On macroscopic scale, all cracks grow on a single plane parallel to the direction of loading. Fracture surfaces exhibit classic initiation-propagation failure regimes, but also completely smooth surfaces such as those observed in quasi-static failures. Moreover, multi-cracking is not present.

The fatigue ratio of A44-24 is around 0.2 similar to A36H96 and A24H96. With all of the above information, it is clear that A44-24, even with average ACN content identical to A36H96, has worse fatigue resistance and it resembles closely the characteristics of A24H96. Perhaps, similar to A24H96, its fatigue resistance and efficiency is better at lower temperatures. However, choice of A44-24 seems a poor one for use at 120 °C.

5 Conclusion

There are relatively few published studies on the fatigue resistance of HNBR. Moreover, studies on the effects of acrylonitrile (ACN) and hydrogenation of HNBR are not available at present to the knowledge of the authors. Thus, in the present extensive study, six different blends of HNBR are investigated at 120 °C. HNBR with 36 wt.-% of ACN and 96 % hydrogenation (A36H96) is taken as the reference. To study the effects of ACN content, two blends with 24 and 44 wt.-% of ACN at constant 96% hydrogenation are considered (A24H96 and A44H96, respectively). Hydrogenation is changed from 91% to 99% at constant 36 wt.-% of ACN (A36H91 and A36H99, respectively). Finally, a composite of 24 wt.-% and 44 wt.-% ACN HNBR for average of 36 wt.-% at constant 96% hydrogenation (A44-24) is used to analyze the effects of blending two HNBRs of different ACN content. The experimental campaign, first, includes fatigue life experiments. The tests are carried out with aid of novel methodologies developed/applied: true stress control and application of the Cox proportional hazards model. Damage mechanism analysis, on macroscopic and microscopic scales, is performed with the use of optical and scanning electron microscopy. Finally, classic crack propagation experiments are carried out.

In terms of fatigue resistance at 120 °C, the reference material A36H96 is the best performing. If ACN content is increased to 44 wt.-%, fatigue resistance slightly degrades (except at stress loads greater than 8.5 MPa); it significantly degrades for ACN content of 24 wt.-%. If hydrogenation is increased to 99% or decreased to 91%, fatigue resistance is also reduced. Overall, it appears that additional hydrogenation does not have a positive impact on fatigue resistance at 120 °C. Finally, the composite A44-24 has lower fatigue resistance than the reference blend it mimics, having similar behavior to A24H96.

As for the perspectives, of course it is important to test the fatigue resistance of these blends in situations that better resemble real-life operational conditions: the effect of oil containing environment on fatigue resistance of HNBR with different ACN content, and the effect of high temperature and/or thermo-oxidative aging on fatigue resistance of HNBR with different percent hydrogenation. The latter is the subject of the upcoming study.

Sources of funding

The present project has received funding from the ANRT (The National Association of Research and Technology of France, CIFRE No.2014/1190) and LRCCP. Tested materials have been manufactured and supplied by LRCCP (60, rue Auber, Vitry-sur-Seine, France).

Conflicts of interest

Any conflict of interest is absent.

References

[1] Tao Z, Viriyabanthorn N, Ghuman B, Barry C, Mead J. Heat resistant elastomers. *Rubber Chem Technol*. 2005;78: 489–515.

[2] Wrana C, Reinartz K, Winkelbach H. Therban (R) - The high performance elastomer for the new millennium. *Macromol Mater Eng*. 2001;286: 657–662.

[3] Hashimoto K, Maeda A, Hosoya K, Todani Y. Specialty elastomers for automotive applications. *Rubber Chem Technol*. 1998;71: 449–519.

[4] Klingender R. *Handbook of Specialty Elastomers*. CRC Press; 2008.

[5] Singha N, Bhattacharjee S, Sivaram S. Hydrogenation of diene elastomers, their properties and applications: a critical review. *Rubber Chem Technol*. 1996;70: 309–367. DOI:10.5254/1.3538435.

[6] Sawada H. Hydrogenated Nitrile Rubber. *Nippon Gomu Kyokaishu*. 1993;9: 653.

[7] Obrecht W, Buding H, Eisele U, Szentivanyi Z, Thörmer J. Hydrierter nitrilkautschuk ein werkstoff mit neuen eigenschaften (in German). *Angew Makromol Chem*. 1986;145: 161–179.

[8] Kim W, Kim M, Chang Y, Shin J, Bae J. Fatigue crack growth behavior of NR and HNBR based vulcanizates with potential application to track pad for heavy weight vehicles. *Macromol Res*. 2003;11: 73–79.

[9] Lacroix F, Tougut A, Neelakantan N, Ranganathan N. A new approach for crack growth life of an elastomeric material. *Procedings of ESIS-ECF 15, Sweden*. 2013; 1–6.

[10] Gauchet S. Etude de l'influence du type de noir de carbone sur la tenue en fatigue de caoutchouc HNBR (in French). *PhD Thesis: Université Francois Rabelais*; 2007.

[11] Narynbek Ulu K. Fatigue of HNBR: effects of formulation and thermal aging. *PhD Thesis: Ecole Centrale de Nantes*; 2018.

[12] Narynbek Ulu K, Huneau B, Verron E, Béranger AS, Heuillet P. On the use of cox regression for statistical analysis of fatigue life results. *J Test Eval*. 2020;48: 1439-1451. DOI: 10.1520/JTE20180541.

[13] Rivlin R, Thomas A. Rupture of rubber. I. Characteristic energy for tearing. *J Polym Sci*. 1953;10: 291–318.

[14] Gent A, Lindley P, Thomas A. Cut growth and fatigue of rubbers. I. The relationship between cut growth and fatigue. *Rubber Chem Technol*. 1964;38: 292–300. DOI:10.5254/1.3535648.

[15] Narynbek Ulu K, Huneau B, Le Gac P, Verron E. Fatigue resistance of natural rubber in seawater with comparison to air. *Int J Fatigue*. 2016;88: 247–256. DOI:10.1016/j.ijfatigue.2016.03.033.

[16] Mars W, Ellul M. Fatigue characterization of a thermoplastic elastomer. *Rubber Chem Technol*. 2017;90: 367–380. DOI:10.5254/rct.17.83780.

[17] Narynbek Ulu K, Huneau B, Verron E, Béranger A, Heuillet P. True stress controlled fatigue life experiments for elastomers. *Int J Fatigue*. 2017;104: 171–182.

[18] Svensson S. Testing methods for fatigue properties of rubber materials and vibration isolators. *Polym Test*. 1981;2: 161–174.

[19] Cox D. Regression models and life-tables. *J R Stat Soc B*. 1972;34: 187–220.

[20] Masquelier I. Influence de la formulation sur les propriétés en fatigue d'élastomères industriels (in French). *PhD Thesis: Université de Bretagne Occidentale*; 2014.

[21] Huneau B, Masquelier I, Marco Y, Le Saux V, Noizet S, Schiel C et al.. Fatigue crack initiation in a carbon black–filled Natural Rubber. *Rubber Chem Technol*. 2016;89: 126–141.

[22] Lake G. Fatigue and fracture of elastomers. *Rubber Chem Technol*. 1995;68: 435–460.

[23] Mars W, Fatemi A. Fatigue crack nucleation and growth in filled natural rubber. *Fatigue Fract Eng Mater Struct*. 2003;26: 779–789.

[24] Diani J, Fayolle B, Gilormini P. A review on the Mullins effect. *Eur Polym J*. 2009;45: 601–612.

[25] Lindley P. Relation between hysteresis and the dynamic crack growth resistance of natural rubber. *Int J Fract*. 1973;9: 449–462.

[26] Lake G, Samsuri A, Teo S, Vaja J. Time dependent fracture in vulcanized elastomers. *Polymer*. 1991;32: 2963–2975.

[27] Mars W, Fatemi A. Observations of the constitutive response and characterization of filled natural rubber under monotonic and cyclic multiaxial stress states. *J Eng Mater Technol*. 2004;126: 19– 28.

[28] Lake G, Lindley P. Mechanical fatigue limit for rubber. *Rubber Chem Technol*. 1965;39: 348–364.

[29] Stephens R, Fatemi A, Robert S, Fuchs H. *Metal Fatigue in Engineering, 2nd ed.*. John Wiley & Sons; 2000.

Supporting information

Supporting information is made available through the online edition of the journal. It contains the following figures:

1. Average stress-strain responses of all tested blends at 120 °C;
2. Schematic for observed crack growth behavior;
3. Micrographs of typical fracture surface categories.